Proceedings of:
ASME TURBO EXPO 2007
May 14-17, 2007, Montreal, Canada

GT2007-27712

Numerical Validations of Secondary Flows and Loss Development Downstream of a Highly Loaded Low Pressure Turbine Outlet Guide Vane Cascade

Johan Hjärne
Department of Applied Mechanics
Chalmers University of Technology
412 96 Gothenburg, Sweden
Johan.hjarne@chalmers.se

Valery Chernoray
Department of Applied Mechanics
Chalmers University of Technology
412 96 Gothenburg, Sweden
valery.chernoray@chalmers.se

Jonas Larsson
Department of Aero and Thermo Dynamics
Volvo Aero Corporation
461 81 Trollhättan, Sweden
jonas.larsson@volvo.com

Lennart Löfdahl
Department of Applied Mechanics
Chalmers University of Technology
412 96 Gothenburg, Sweden
lennart.lofdahl@chalmers.se

ABSTRACT

In this paper 3D numerical simulations of turbulent incompressible flows are validated against experimental data from the linear low pressure turbine/outlet guide vane (LPT/OGV) cascade at Chalmers in Sweden. The validation focuses on the secondary flow-fields and loss developments downstream of a highly loaded OGV.

The numerical simulations are performed for the same inlet conditions as in the test-facility with engine-like properties in terms of Reynolds number, boundary-layer thickness and inlet flow angles with the goal to validate how accurately and reliably the secondary flow fields and losses for both on- and off-design conditions can be predicted for OGV's.

Results from three different turbulence models as implemented in FLUENT, k-ε Realizable, kω-SST and the RSM are validated against detailed measurements. From these results it can be concluded that the RSM model predicts both the secondary flow field and the losses most accurately.

1 INTRODUCTION

The aerodynamic function of the low pressure turbine outlet guide vanes (LPT/OGV) is to turn the swirling flow from the last low-pressure turbine rotor into an axial flow for the design point with lowest possible pressure loss. This de-swirling generates a diffusing flow with growing boundary layers, strong secondary flows, and increases the risk of separation on the vane surfaces as well as the hub and shroud. In addition to this the OGV should also perform without big pressure losses or separation in off-design conditions which makes the design procedure even more challenging. In terms of turbulence modeling this is a difficult case to predict and an experimental basis for code validation is needed.

Losses due to secondary flows are a considerable part of the total losses for the flow around OGV's. Because of this the understanding of secondary flows is very important for the reduction of total losses and also for the optimized efficiency for the OGV's. In today's development of civil jet engines cost and weight requirements lead to more highly loaded turbines with fewer stages. In un-geared two and three shaft engines, this gives higher swirl angles into the OGV which lead to a higher loading for the OGV. The increased loading leads to stronger secondary flows which make it even more important to study these effects.

Most of the literature concerning cascade secondary flows is dedicated to turbine flows, excellent publications have been provided by Sieverding [1] and later by Wang et al. [2] and Goldstein and Spores [3] amongst others. In these papers fundamentals of secondary flows in cascades are discussed which not will be the case in this paper, which instead puts its focus on the numerical validation. However Hjarne et al. [4] showed that there are differences in the downstream evolution of the secondary flow structures between turbine types of cascades and an OGV cascade, mainly due to the lower loading for the OGV.

The aim of this paper is to present how three well known turbulence models, in the turbomachinery field, predict the secondary flow field as well as to evaluate the performance with downstream distance of an OGV cascade. This will be done for three different flow angles, 20, 30 and 40 degrees, and fixed other conditions.

NOMENCLATURE

C	blade chord [m]
Cp	pressure coefficient
P_s	static pressure [Pa]
P_{tot}	total pressure [Pa]
P_{dyn}	dynamic pressure [Pa]
Re_c	Reynolds number based on chord length

U, V, W	mean velocity components in x, y and z-direction [m/s]
x, y, z	coordinates [m], see Fig. [1]
y^+	dimensionless wall distance

Greek Symbols

δ_{099}	boundary-layer thickness [m]
ω_x	streamwise vorticity [1/s]
ξ	total pressure loss [%], see Eq. [1]

Subscript

mwa	mass weighted average
in	inlet conditions
pitch	pitchwise

Acronyms

LPT	low pressure turbine
OGV	outlet guide vane

2 EXPERIMENTAL SETUP

The linear cascade used for these measurements is an open circuit blower type. As Fig.1 illustrates the test section is built up of two parallel discs and two blade carriers, with the blade carriers constituting the side walls of the 7 OGV's, thus forming the cascade. The gap between the inner and outer discs is used for sucking out the boundary layers developed in the upstream sections. A 30 kW fan is used to drive the flow through a diffuser and a flow conditioner (consisting of a honeycomb and three screens with different porosity). The turbulence grid was placed 450mm upstream of the cascade and parallel to the leading edge plane, see Fig. 1. This grid increases the turbulence intensity from 0.5% to 5%. A more detailed description of the test-facility has been given earlier by Hjärne et al. [5, 6].

The OGV geometry used for these investigations has been developed at Chalmers as a demonstrator for OGV validation cases. The OGV consists of a 2D profile section which is extended in the span direction, see Fig. 2. The design requirement for this vane is to turn the incoming flow with an inlet flow angle of 30 degrees to an axial outflow and the off-design requirements are ± 10 degrees incidence without total mid-span separation. The static pressure around the OGV's is measured with pressure taps, see Fig. 2. The geometrics of the OGV and the flow conditions are presented in table 1.

Significant efforts were made to obtain a good flow periodicity in the cascade. The flow periodicity has been checked for all inlet flow angles and is illustrated for the design case in Fig. 3 which shows the Cp distribution for the three mid OGV's in the cascade. The variation from one OGV to another is small both on the pressure side and on the suction side. In Fig. 4 the loading for the three different inlet angles is shown and for the highest inlet flow angle the loading is very high with the suction peak close to the leading edge of the blade. Figure 4 also demonstrates that the symmetry of the flow in the test section was good which is shown by the six additional control points positioned at 25% and 75% span on the OGV. For further details both the symmetry and periodicity for the different load cases have been discussed in earlier papers by Hjarne et al., see [4, 6 and 7].

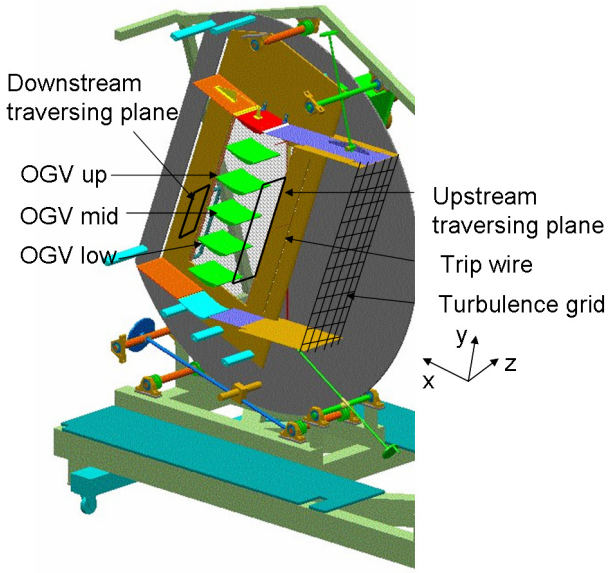

Figure 1 Drawing of experimental set up.

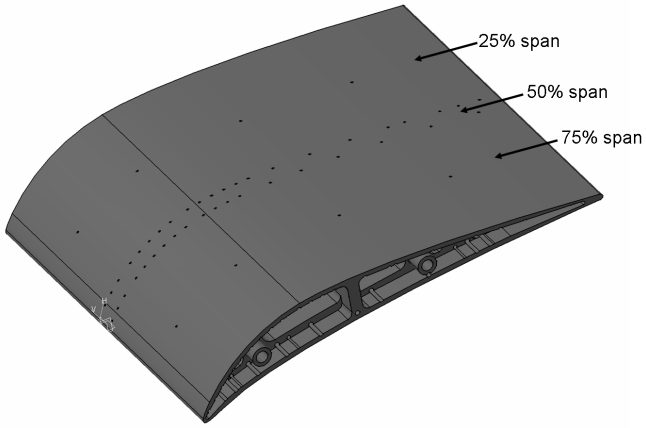

Figure 2 Location of suction side pressure taps for the OGV.

Table 1 Cascade geometry data

Number of vanes	7
Chord length (mm)	220
Pitch to chord ratio	0.91
Aspect ratio (Span to Chord ratio)	0.91
Inlet velocity (m/s)	20
Inlet Reynolds number	280000
Inlet flow angles (°)	20,30,40
Turbulence intensity (%)	5
Incoming boundary layer, δ_{099} (mm)	9.6

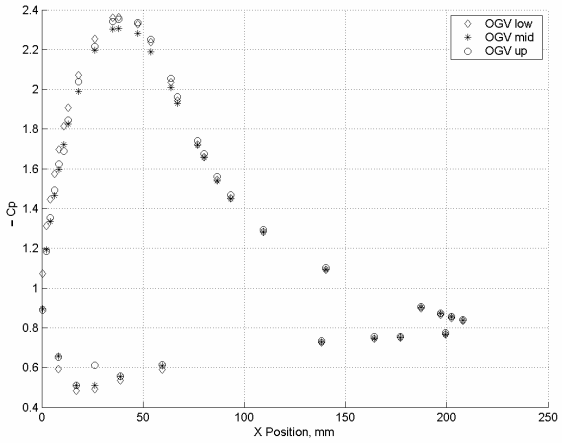

Figure 3 Cp distributions for mid sections of three OGV's for the design case.

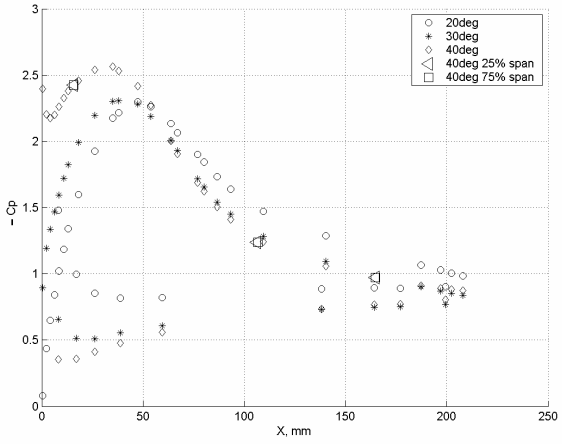

Figure 4 Cp distributions on the mid vane for three different load cases.

Instrumentation and measurements

Two traversing systems have been used to measure the flow field both upstream and downstream. The movements in the (y, z) plane are controlled by stepper motors with an accuracy of at least 12.5μm. The five-hole pressure probes used for the upstream and downstream traverses have been manufactured at Chalmers and were calibrated between –20 to 20 degrees for both pitch and yaw angles. The size of the probe head diameter was 3.5 mm with an individual distance between the holes of 2 mm.

For the design-point the cross wire (x-wire) probe was used for the downstream flow measurements as well. The standard Dantec's x-wire probe was equipped with gold plated 5-μm wires of 1.2 mm active length. The probe was calibrated at velocities between 2 and 35 m/s and flow incidence angles between -45 and 45 degrees.

The inlet measurements were conducted at an axial position of -30% chord upstream the cascade inlet plane with a resolution of the flow field of 20mm (10% pitch) in y and z direction. The upstream traversing system, equipped with a hot-wire probe, was also used to measure the incoming boundary layer height along the side walls. For correct experimental modeling it is important to maintain the incoming boundary layers at similar thickness as in a real gas channel. Since the aspect ratio of the OGV is rather low and the flow field is diffusive a too thick or thin incoming boundary layer will affect both the separation margins and the secondary flow field. Therefore the side wall boundary layers were tripped with a 1.5 mm wire placed 1.36*C in the flow direction in front of the blade leading edge plane. The boundary layer was measured in the flow direction 0.91*C upstream of the leading edge plane, it was fully turbulent and had a thickness of 9.6mm (δ_{099}).

As the test rig has very good symmetry, the outlet measurements were taken over half of the span one pitch length over the central blade (140mm below the trailing edge to 60mm above the trailing edge) at three different streamwise locations downstream of the trailing edge (0.25*C, 0.5*C and 0.8*C). An experimental grid of 2mm in each direction was used. To avoid wall proximity effects, as suggested in [8], the flow field was not measured at a distance closer than two times the five-hole probe head size from the endwall. The same measuring planes were used for both the five-hole probe and the x-wire probe measurements.

3 NUMERICAL CALCULATIONS

The 3D CFD calculations are preformed with the numerical software tool FLUENT [9] (version 6.2.16). Three different turbulence models, k-ε Realizable, k-ω SST, and the RSM model have been used and compared with experimental results.

The mesh generator used was ICEM-HEXA and a side view of the computational domain for the calculations is depicted in Fig. 5. The inlet boundary condition was placed 0.9*C upstream of the blade leading edge and the outlet boundary condition was placed 0.9*C downstream of the trailing edge.

A mesh dependence study was performed using two different mesh sizes. The baseline mesh had $6.9*10^5$ mesh cells and the refined mesh had $1.35x10^6$ cells. The turbulence model used for this study was the k-ε realizable with resolved boundary layers.

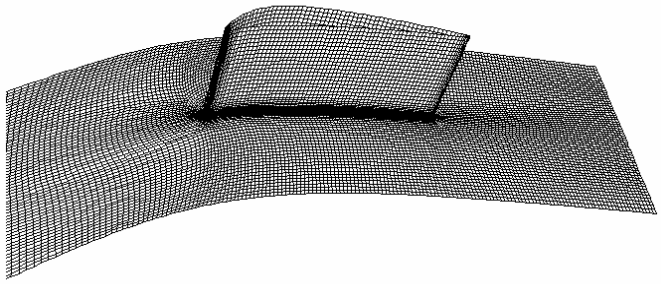

Figure 5 Baseline 3D mesh consisting of $6.9*10^5$ cells.

To check the grid sensitivity the mass averaged total pressure losses over the OGV, ξ_{mwa}, were calculated at 3 positions 0.25*C, 0.5*C and 0.8*C downstream the trailing edge of the OGV. Figure 6 compares the total pressure loss for the two meshes and the maximum difference was found to be 0.015%. Therefore the baseline mesh was considered to be

sufficiently refined in order to obtain results which were independent of the grid.

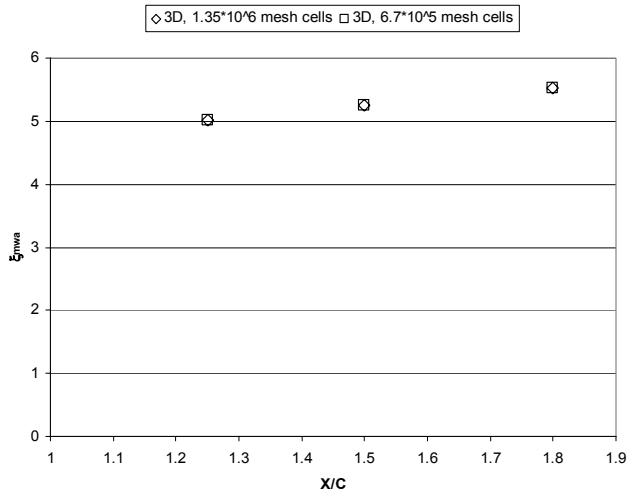

Figure 6 Mesh sensitivity study of total pressure loss at different downstream positions.

Turbulence Modeling

The aerodynamic function of the OGVs is both to turn the swirling flow from the last LPT-rotor into an axial direction and to recover the static pressure. This de-swirling yields a diffusive flow with growing boundary layers, strong secondary flows, and increases the risk of separation on the vane surfaces as well as on the side walls. In terms of turbulence modeling this is a challenging case to predict.

Shih's realizable k-ε model [10]

This is the most commonly used turbulence model in FLUENT. It is similar to the classical k-ε model but has a variable C_μ and a modified ε equation. The main advantage with the Realizable version for the present application is that it has better performance, in terms of predicting the production of k, compared to a classical k-ε model in regions with strong deceleration and acceleration, for example in the leading edge region and the region around the suction side pressure minimum. This is a high-Re model which needs to be complemented with a low-Re model close to the walls if a grid with resolved boundary layers is used.

Menter's SST k-ω model [11, 12]

This model has become increasingly popular in the last few years and it is now regarded as a standard model in the turbomachinery field. It is a low-Re model which performs well with resolved boundary layers. The SST k-ω model has been known to work especially well for cases with adverse pressure gradients and separations. It is also commonly used in heat-transfer applications.

RSM [13, 14, 15]

The Reynolds Stress Models solves the Reynolds stresses using individual transport equations. This model accounts for the effects of streamline curvature and rapid changes in the strain rate in a more rigorous manner than the two equation models and therefore it has a good potential to give accurate predictions for the flow under consideration.

In addition to the abovementioned turbulence models an enhanced near-wall treatment was used.

Enhanced wall-treatment/two-layer model [16, 17, 18]

When used on fine grids with resolved boundary layers ($y^+ < 1$) this model employs a Wolfstein [16] one-equation model in the inner parts of the boundary layers. This model is matched to the k-ε model in the outer region following the work by Jongen [17]. The length-scale is computed according to Chen & Patel [18]. This two-layer approach is very attractive. It avoids the ad-hoc damping functions used in many other low-Re models and it seldom leads to any numerical problems. For cases with large separations and 3-dimensional boundary layers, the low-Re two-layer model is normally superior to a wall-function approach.

The FLUENT simulations were computed for incompressible, viscous, low-speed conditions with inlet velocity profiles taken from the measurements. All calculations where conducted with resolved boundary layers and were performed with a segregated double precision solver and a second order upwind scheme. The y^+ mean value on the OGV were 0.2.

4 RESULTS AND DISCUSSION

Complete investigations of an OGV downstream passage were made with a 5-hole pressure probe. Three different downstream positions were monitored for three different inlet flow angles. A time mean value of the flow field variables was deduced and with a high plane discretization it was possible to compute the streamwise vorticity. The vorticity field allows for a better understanding of the development of the secondary flows.

To ensure that the results from the 5-hole probe are both reliable and accurate additional x-wire probe measurements were made at the on-design point. These results were obtained after the 5-hole probe measurements using the same probe positioning and mapping for the same flow conditions. The results are very similar which increases the reliability of both experiments and also makes them good suited as validation cases for numerical codes.

Comparison, x-wire → 5-hole probe (inlet flow angle = 30deg)

In Fig. 7 measurement results from both the 5-hole probe and the x-wire probe are presented. The calculated vorticity in the streamwise direction is shown at the distance 0.5*C downstream of the trailing edge. As can be seen the results are almost identical. Examining the plots the same characteristics are visible in each plot. Starting with the boundary-layer vorticity (blue region on the side wall) it has the same thickness and intensity in both cases. The boundary layer is also seen to increase in thickness from the pressure side to the suction side which is due to the pressure gradient in the same direction. The top bulge in the boundary layer (rotating clockwise) is referred to as the passage vortex. This vortex is developed from the flow in the side wall boundary layer, when this flow hits the suction side of the OGV it rolls up to form a vortex. In Fig. 7 it is shown how the boundary-layer vorticity feeds the passage vortex and also how the passage vortex pushes the counter clockwise rotating red region, referred to as the blade shed vorticity, towards mid span. This vorticity is produced by the shedding motion of the fluid towards the OGV. The magnitudes

of the secondary flow structures are very similar, with the same magnitudes being visible in the same positions.

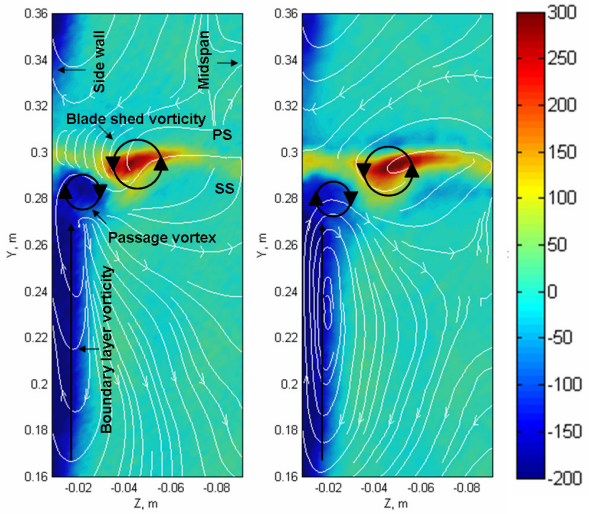

Figure 7 Comparison of streamwise vorticity from the 5-hole probe measurements (left) and from the x-wire measurements (right) with superimposed streamlines.

Considering the differences in the measuring techniques for the two probes, the results are very comparable, all the major structures are present in both sets of plots, the trailing edge vortex sheet, the passage vortex and the side wall boundary layer vorticity. Although there are some differences they are only minor and do not affect the reliability of the result in either case. The main reason for the differences is due to the x-wire probe being better suited to measure flow fields with high velocity gradients, and that the x-wire probe was almost half the size of the 5-hole probe. Because of these two facts it is harder for the 5-hole probe to determine vortical structures. As is seen in Fig. 7 the x-wire measures a well-defined vortex in the boundary layer region which is not present in the plot for the 5-hole probe. There is a well-known drawback of using 5-hole probes in gradient flows, which comes from the finite distance between the holes. For example, when the probe is traversed in the pitch direction (y-direction) the top and bottom hole of the probe will always be in different parts of the wake making an artificial vertical velocity component gradient. With increase of the distance from the trailing edge the similarities between the two measurement methods are improved which is because of the decreasing velocity gradients.

Measurements vs. calculations (α = 30deg)

Figures 8-10 compare the streamwise vorticity and the two velocity components that constitute the streamwise vorticity, the v-velocity component and the w-velocity component. All plots are presented at a distance of 0.5*C downstream of the trailing edge. From left to right the figures show measurements by the 5-hole probe, measurements by the x-wire probe, calculations by the realizable k-ε model, the kω-SST model and the RSM model.

Studying the results in Fig. 8 there are several interesting effects to notify. All major flow patterns are captured by the three models such as the boundary-layer vorticity close to the end-wall, the passage vortex and the blade shed vorticity. The kω-SST and the RSM models predict these patterns better compared to the realizable k-ε which seems to be the most diffusive model. The RSM model shows the correct position of both the passage vortex and the blade shed vorticity as in the experiments. Looking at the kω-SST results it is noticeable that the position of the locus of the blade shed vorticity is lower both compared to the RSM model and to the experiments. This is due to that the kω-SST model predicts a separation at the suction side starting just behind the suction peak and stretches towards the trailing edge. This separation pushes the blade shed vorticity downwards. Figure 11 shows the different degrees of suction side separation predicted by the different models for the on-design case.

Looking at the streamlines in Fig. 8 small differences are seen between the two experiments and the calculations. The calculations all show a similar flow pattern which is very comparable to the experiments. Both the feeding of the passage vortex from the boundary-layer vorticity and the interaction between the passage vortex and the blade shed vorticity is clear. The only noticeable difference is the vorticity core in the boundary layer region in the RSM solution. This core is also visible in the x-wire experiment but in this case closer to the suction side of the vane. This vortex arises due to the interaction between the movement of the flow in the boundary layer and in the free stream.

The major difference between the experiments and the calculations are the magnitudes of the streamwise vorticity. None of the models predict the same magnitudes as described by the two experiments. The RSM model is closer to the experiments compared to the other two models but the magnitudes of the main structures are still lower compared to the experiments. Even though the calculations are carried out with inlet properties obtained in the measurements it can be seen that the calculations do not manage to predict the correct velocity components in y and z direction.

To explain the differences between the different levels in the streamwise vorticity the V- and W-velocity components must be studied in more detail. Starting with the V-velocity component in Fig. 9 it is clear that all models underpredict the extent of the positive V-velocity component in the region close to the side wall. This is obviously the reason of the underprediction of the boundary layer vorticity and the intensity of the passage vortex in the calculations. Again it is the RSM calculation that is closest to the experiments and predicts the velocity distribution near the side wall best compared to the two other models. Also the negative velocity spot positioned close to the core of the blade shed vorticity appears in the correct position but again the magnitude is too low. The results for the kω-SST model are comparable to those for the RSM model.

In Fig. 9 it is also visible that the 5-hole probe does not measure the V-component well in the wake due to the finite spatial distance between the probe holes. The 5-hole probe measures both a region of negative and positive velocity along the entire span which not is the case for the x-wire probe measurements nor the calculations. Nevertheless the streamwise vorticity is predicted remarkably well and once again these results support the fact that the vorticity representation of the 5-hole probe data is the most correct for examining the flow structure.

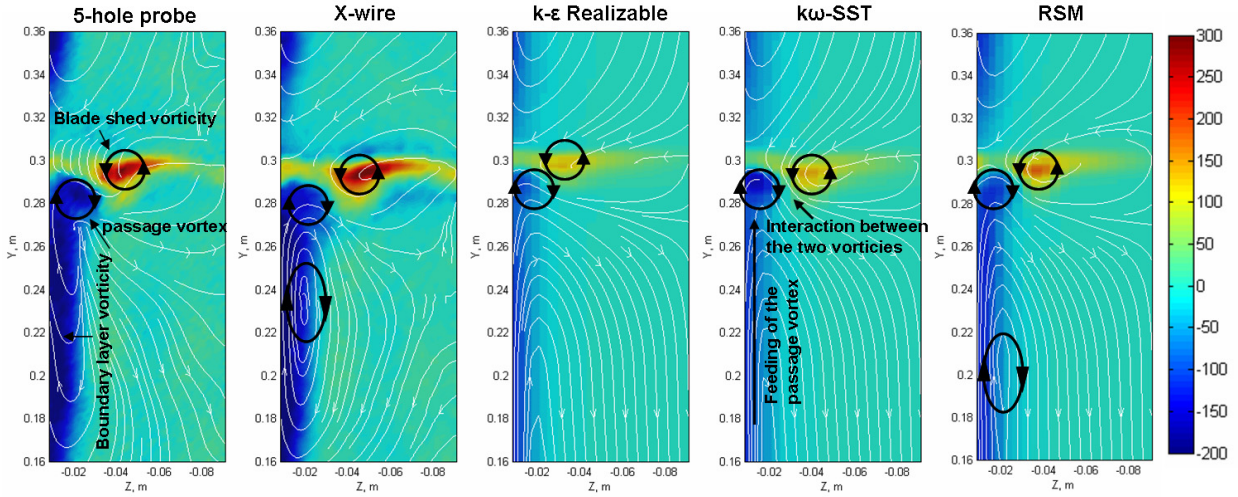

Figure 8 Streamwise vorticity for the design case (inlet flow angle 30º) plotted downstream at position X=0.5*C.

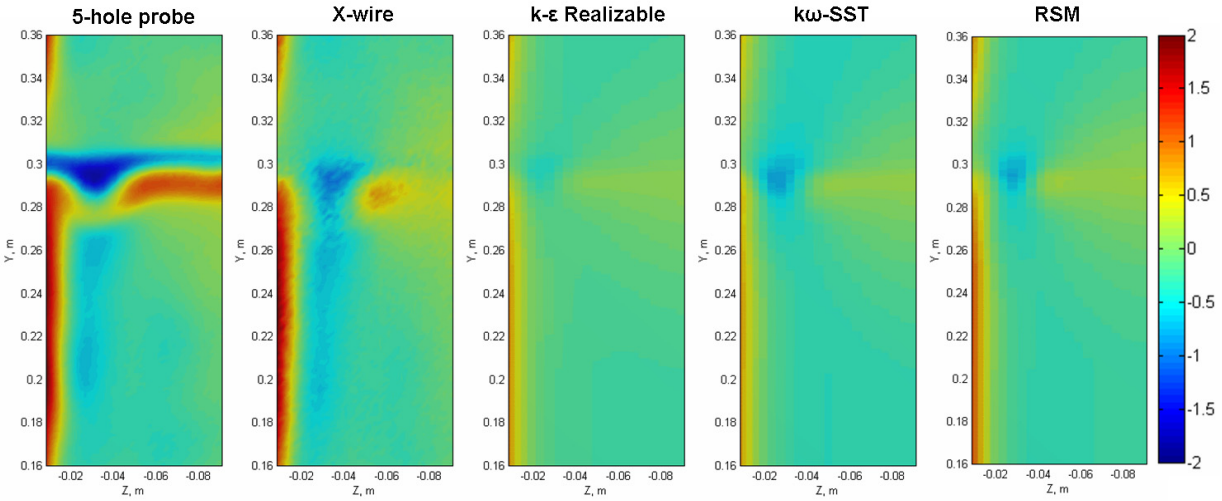

Figure 9 V-velocity component for the design case (inlet flow angle 30º) plotted downstream at position X=0.5*C.

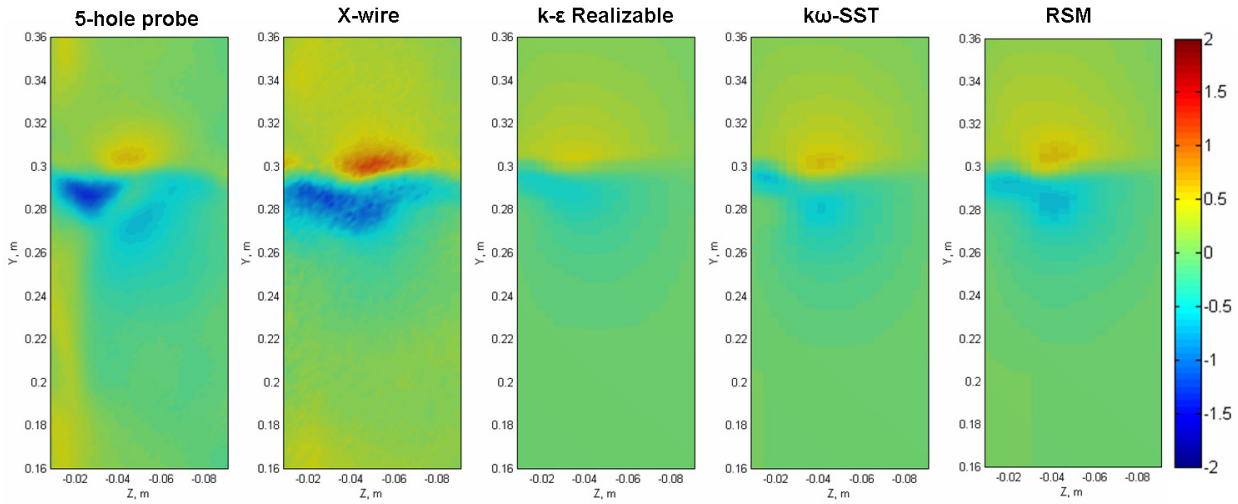

Figure 10 W-velocity component for the design case (inlet flow angle 30º) plotted downstream at position X=0.5*C.

The W-component is described in Fig. 10. Again the models underpredict the intensity of the velocity component but the main patterns are fairly well predicted by the numerical models.

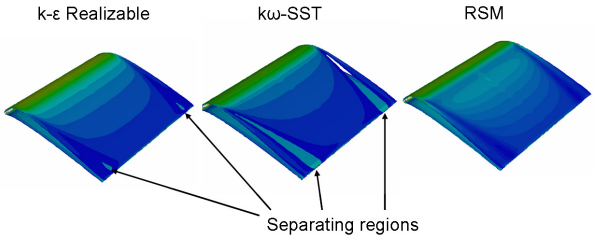

Figure 11 Positive x-wall shear stresses at the suction side showing the different levels of separation for the design case.

The plots presented in Fig. 8-10 are good for visualizing the flow pattern of the secondary flow field and to understand its spatial distribution. To get a more quantitative comparison Fig. 12 shows the pitchwise average of the streamwise vorticity plotted along the span at 0.5*C downstream of the trailing edge. As already shown above the similarity between the two experiments is very good and they both predict the similar distribution of the average streamwise vorticity along the span. Closest to the wall the extension of the negative vorticity from the boundary layer is slightly lower for the 5-hole probe measurement compared to the x-wire. This difference can be explained by the wall proximity affecting the 5-hole probe measurements close to the wall Apart from this an almost identical distribution is seen from the two experiments.

The calculations show some differences compared to the experiments. The realizable k-ε and the kω-SST models show fairly the same distribution from the wall to the mid span but with lower levels of the boundary-layer vorticity. Slight differences can be seen where the kω-SST is somewhat closer to the experiments, especially for the blade shed vorticity which is predicted at the correct location. The biggest difference between the RSM and the other models is the region close to the side wall where the RSM model predicts the spanwise location of the vorticity extreme farther from the wall. As is seen the vorticity magnitude near the side wall is about 40% underpredicted by the calculations.

Measurements vs. Calculations for off-design conditions (α = 20deg, 40deg)

When the inlet flow angle is changed this also changes the loading of the guide vane and secondary flow patterns are highly dependent on the loading. For this OGV it means that the OGV should deflect an inlet flow angle in the range between 20 to 40 degrees without a total mid-span separation.

Figure 13 shows how the streamwise vorticity is distributed for an inlet flow angle of 20 degrees. For this inlet flow angle the magnitudes are much better predicted. From the wall region all the models predict the same vorticity level as the 5-hole probe experiment. At this inlet condition the RSM model captures the extension of the vorticity field better compared to the other models especially in the boundary layer region.

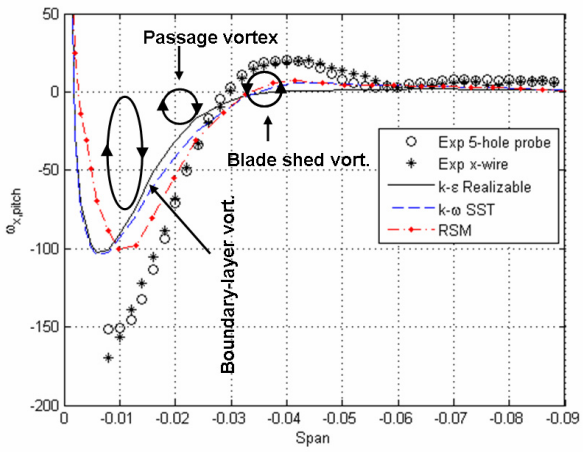

Figure 12 Pitchwise average of the streamwise vorticity at X=0.5*C downstream of the trailing edge.

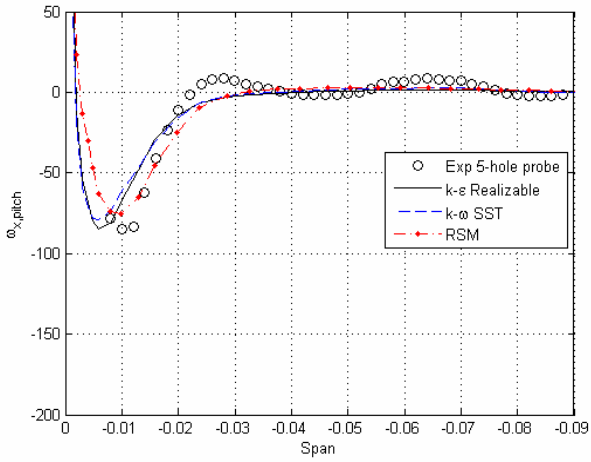

Figure 13 Pitchwise average of the streamwise vorticity at X=0.5*C for an inlet flow angle of 20 degrees.

When the inlet angle is increased to 40 degrees it was found that all models predicted separation in the corner between the suction side and the side wall with varying extension towards mid span, see Fig. 14. The separation for the kω-SST model was bigger compared to the other models and covered most of the suction surface.

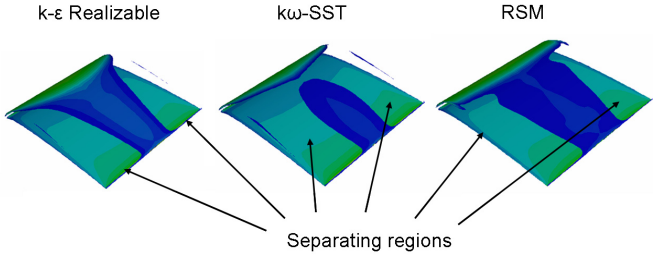

Figure 14 Positive x-wall shear stresses at the suction side showing the different levels of separation for the highest load case.

As seen in Fig. 15 the magnitudes of the vorticity are now significantly underpredicted and for this flow-case the flow structure is not resolved that well as for the lower flow angles. Compared to the experiments all the models underpredict the extension of the boundary-layer vorticity, which probably is due to the large corner separations predicted by all the models. For the blade shed vorticity it is only the RSM model that predicts it good even though it misses its locus this model predicts vorticity of the same level.

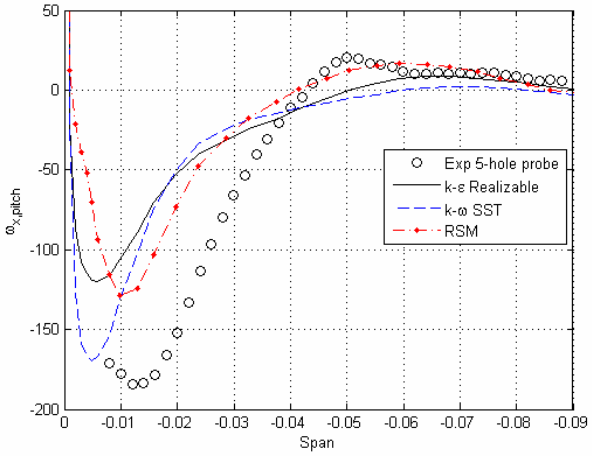

Figure 15 Pitchwise average of the streamwise vorticity at X=0.5*C for the inlet flow angle of 40 degrees.

Losses

The pitchwise average total pressure loss distribution at the downstream position 0.5*C is shown in Fig 16 and in Fig. 17 the total mass weighted averaged loss is presented for all three downstream positions. The losses are calculated with respect to the inlet pressure values, see Eq. (1).

$$\xi = \frac{P_{tot} - P_{tot,in}}{P_{dyn,in}} \qquad (1)$$

The losses for the design flow case are very well predicted by all three models and the RSM show the same distribution as the experiments in the near wall region. The unloading in the experiment after the blade shed vorticity is most probably due to transition on the suction side. Simple oil flow visualizations showed a laminar separation bubble close to the suction peak.

The mass weighted average of total pressure loss at all three downstream positions is shown in Fig. 17, which demonstrates very good agreement with the experiments especially for the first two downstream axial positions. Interesting to notice is that for the integrated losses k-ε realizable model is closest to the experimental results with an underprediction at the first and last position and a slight overprediction at the mid axial position. The other two models show the exact same loss prediction for all three downstream positions and at all locations they underpredict the losses. The large difference for the furthest downstream station is most probably caused by a measurement error or by the fact that this station is very close to the outlet of the facility. Thus this measurement point is shown in brackets.

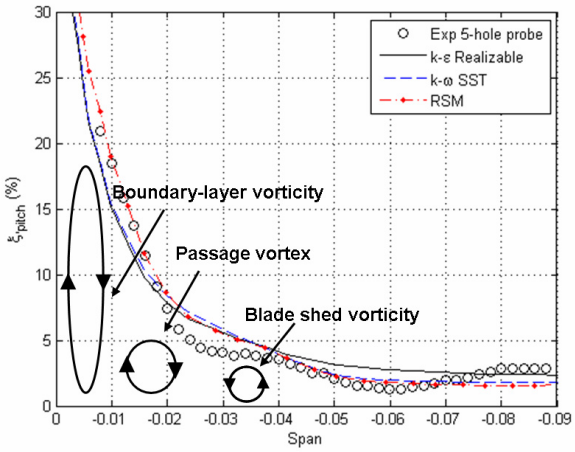

Figure 16 Pitchwise average of the losses for the design case at X=0.5*C.

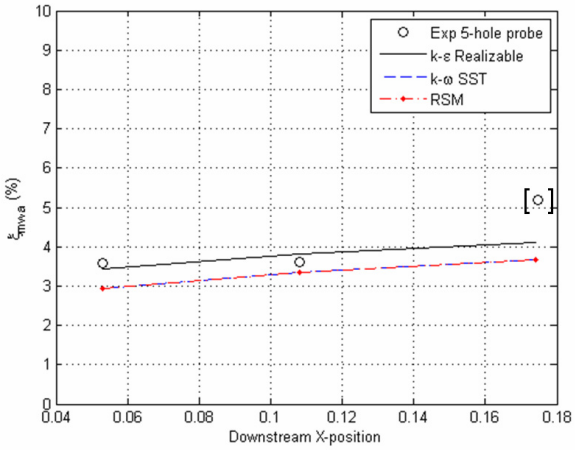

Figure 17 Evolution of the mass weighted averaged losses at the three downstream positions for the on-design case.

In Fig. 18 and 20 the losses are shown for the inlet flow angle of 20 degrees. The pitchwise averaged losses are again captured well compared to the experiments as in the previous case. All the models predict similar results and the biggest difference is that they show a smoother curve compared to the experiment. The trend is similar and at mid span all models predict the same results as the experiment. The obvious difference is the spanwise oscillation in the experiment, where the loss distribution is almost zero at span = -0.05. Looking closely a similar but weaker wavy pattern is captured by the kω-SST model. The possible explanation for this is a separation and reattachment on the leading edge pressure side. This phenomenon is captured by the kω-SST model and shown in Fig. 19. The separation creates two streaks of lower x-wall shear stress after the separation which affects the P_{tot} wake and creates a minimum in the pressure losses. The effect of thinner sections in the P_{tot} wake was also seen in the experiment.

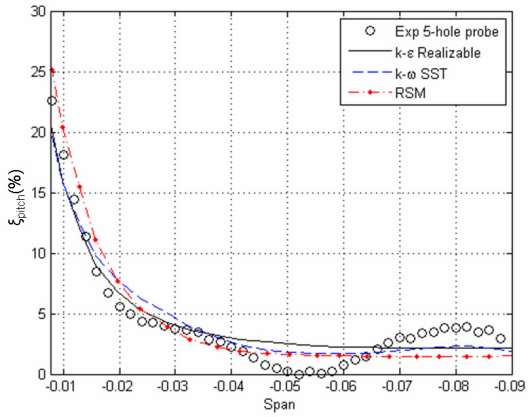

Figure 18 Pitchwise average losses for an inlet angle of 20 degrees at X=0.5*C downstream of the trailing edge.

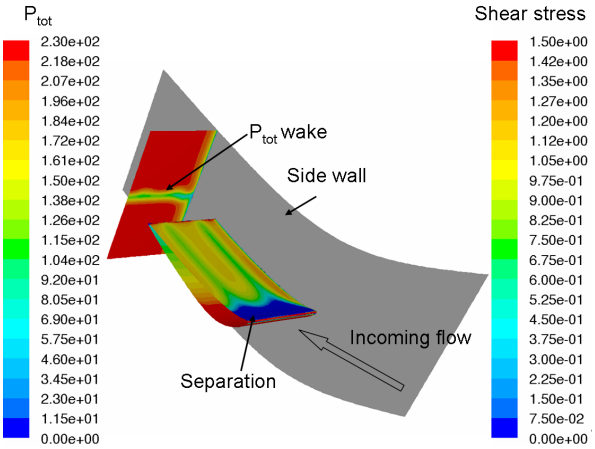

Figure 19 The separation on the leading edge pressure side creates two streaks of lower x-wall shear stress that affect the P_{tot} wake.

Fig. 20 shows the total loss for the three downstream positions and except for the first downstream position the results are very similar. For the latter two positions the realizable k-ε model is closest to the experimental results with slight underpredictions. The kω-SST and the RSM underpredict the losses somewhat more.

The losses for the highest load case are shown in Fig. 21 and 22. As mentioned earlier all the models showed significant suction side separations for this flow case and therefore the results are varying. Starting with the spanwise distribution shown in Fig. 21 it can be seen that the only turbulence model that predicts the same trend as the experiment is the RSM model. However the magnitudes differ significantly. The model that suffers the most from the separation is the kω-SST model which shows the biggest deviation. The fact that the kω-SST model is sensitive for separation has been verified earlier for mid span properties by Hjane et al. [7].

Finally Fig. 22 shows the mass averaged downstream losses for various axial positions. As in the case of the pitchwise average the numerical results differs remarkably from the experimental results. Also here it is the RSM model that is closest to the experimental results. But even this model overpredicts the losses by more than 50%.

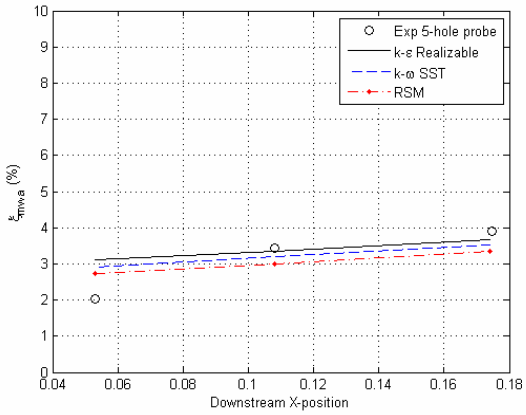

Figure 20 Mass weighted averaged losses at an inlet flow angle of 20 degrees.

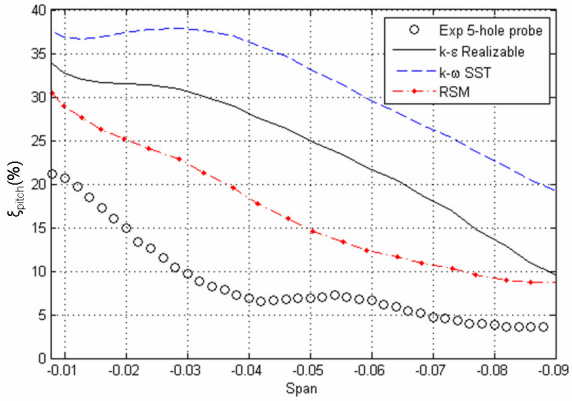

Figure 21 Pitchwise average losses for an inlet angle of 40 degrees at X=0.5*C downstream of the trailing edge.

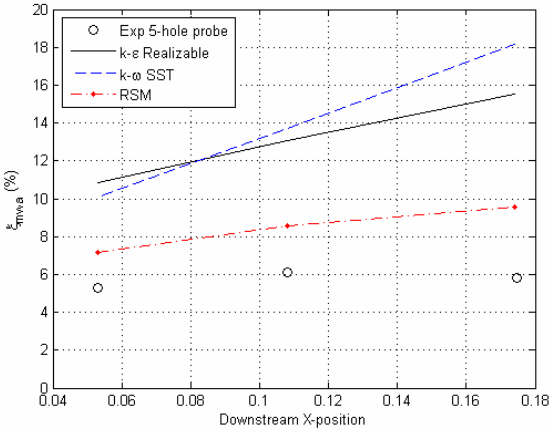

Figure 22 Mass weighted averaged losses at an inlet flow angle of 40 degrees.

5 CONCLUDING REMARKS

In this paper a complete investigation of the downstream secondary flow field for a low pressure turbine outlet guide

vane cascade has been analyzed with two different experimental techniques. The two different experiments showed very similar results both considering the distribution of the secondary flow field and also the impact of the secondary flows on the downstream losses. Therefore the experiments constitutes as good validation cases for turbulence models. The main conclusions drawn in this paper are:

Design case (30 degrees inlet flow angle)

The RSM model predicts secondary flow structures most correctly for the design case. Even though the magnitudes differ all the major secondary flow characteristics are visible. The spanwise and total pressure losses are also well predicted.

The result for the kω-SST model is similar to the RSM but because of a predicted corner separation already at the design case they differ slightly at both the secondary flow field and downstream losses.

The k-ε Realizable seems to be the most diffusive model and predict the secondary flow field worse compared to the other two models. The mass weighted average losses are however well predicted compared to the experiments.

Off-design case (20 degrees inlet flow angle)

For the lower inlet flow angle both the secondary flow field and the loss distribution were very well predicted by all the three models. In this case the level of the streamwise vorticity agreed well with the experiment and the RSM model was slightly better than the other models. Considering the mass averaged outlet losses the k-ε realizable model was again closest to the experiment.

Off-design case (40 degrees inlet flow angle)

For this inlet flow angle all the numerical models showed different sizes of separation on the suction side of the OGV. This is clear when comparing both the secondary flow field and the losses. Again the RSM model was closest to the experimental results. Even though it is quite far off from the experiments it is the only model that captures the correct trends.

As a final summary all the turbulence models are able predict the downstream evolution of the secondary flow field. The main differences compared to the experiments are the intensity in the vorticity which differ more while increasing the loading. Overall the RSM model predicts the secondary flowfield more accurately compared to the other two models and if detailed information about secondary flows is to be determined this model is recommended.

ACKNOWLEDGEMENTS

The present work is a part of the project COOL supported by the Swedish Gas Turbine Center (GTC), and funded by Siemens, Volvo Aero Corporation and Energimyndigheten. The permission for publication is gratefully acknowledged. The authors would also like to thank Stefan Kennedy for his help with the x-wire measurements.

REFERENCES

[1] Sieverding, C. H., 1985 "Recent Progress in the Understanding of Basic Aspects of Secondary Flows in Turbine Blade Passages," Transactions of the ASME, Vol. 107

[2] Wang, H. P., Olson, S. J., Goldstein, R. J. and Eckert, E.R.G., 1997 "Flow visualization in a Linear Turbine Cascade of High Performance Turbine Blades," Journal of Turbomachinery, Vol. 119

[3] Goldstein, R. J. and Spores, R. A., 1988 "Turbulent Transport on the Endwall in the Region Between Adjacent Turbine Blades," Transactions of the ASME, Vol. 110

[4] Hjärne, J., Larsson, J. and Löfdahl, L., 2006, "An Experimental Investigation of Secondary Flows and Loss Development Downstream of a Highly Loaded Low Pressure Turbine Outlet Guide Vane Cascade," ASME paper GT2006-90561

[5] Hjärne, J., Larsson, J. and Löfdahl, L., 2003, "Design of a Modern Test-Facility for LPT/OGV flows," ASME paper GT2003-38083

[6] Hjärne, J., Larsson, J. and Löfdahl, L., 2005, "Experimental Evaluation of the Flow Field in a State of the Art Linear Cascade with Boundary-Layer Suction," ASME paper GT2005-68399

[7] Hjärne, J., Larsson, J. and Löfdahl, L., 2006, "Performance and Off-Design Characteristics for Low Pressure Turbine Outlet Guide Vanes: Measurements and Calculations," ASME paper GT2006-90550

[8] Arts, T., Boerrigter, H., Buchlin, J.-M., Carbonaro, M., Degrez, G., Dénos, R., Fletcher, D., Olivari, D., Riethmuller, M.L., Van den Braembussche, R.A., "Measurement Techniques in Fluid Mechanics", 2nd revised edition, reprint of VKI LS 1994-01.

[9] FLUENT 6, 2001, Users manual, Fluent Incorporated, Lebanon, NH, USA

[10] Shih, T.-H., Liou, W. W., Shabbir, A. Z., Yang, and Zhu, J., 1995, "A New Eddy-Viscosity Model for High Reynolds Number Turbulent Flows - Model Development and Validation", *Computers Fluids*, 24(3), pp 227-238

[11] Menter, F. R., 1994, "Two-Equation Eddy-Viscosity Turbulence Models for Engineering Applications", *AIAA Journal*, 32(8), pp 1598-1605

[12] Menter, F. R., Kuntz, M. and Langtry, R., 2003, "Ten Years of Experience with the SST Turbulence Model", in Hanjalic, K., Nagano, Y. and Tummers, M., editors, *Turbulence, Heat and Mass Transfer 4*, pp 625-632, Begell House Inc.

[13] Gibson, M. M. and Launder, B. E., 1978, “Ground Effects on Pressure Fluctuations in the Atmospheric Boundary Layer”, 1978, *J. Fluid Mechanics*, 86 pp 491-511.

[14] Launder, B. E., “Second-Moment Closure: Present and Future?”, 1989, *Int. J. Heat Fluid Flow*, 10(4) pp 282-300.

[15] Launder, B. E., Reece, G. J. and Rodi, W., 1975, “Progress in the Development of a Reynolds-Stress Turbulence Closure”, 1975, *J. Fluid Mechanics*, 68(3) pp 537-566.

[16] Wolfstein, M., 1969, “The Velocity and Temperature Distribution of One-Dimensional Flow with Turbulence Augmentation and Pressure Gradient”, *Int. J. Heat Mass Transfer*, 12 pp 301-318.

[17] Jongen, T., “Simulation and Modeling of Turbulent Incompressible Flows”, 1992, PhD thesis, EPF Lausanne, Lausanne, Switzerland.

[18] Chen, H. C. and Patel, V. C., 1988, “Near-Wall Turbulence Models for Complex Flows Including Separation”, *AIAA Journal*, 26(6):641-648.